Doping Profile Extraction for Predictive Modeling of Single Photon Avalanche Diodes

Andrea Bonzi, Gabriele Laita, Ivan Rech, *Senior Member, IEEE*, and Angelo Gulinatti, *Member, IEEE*

***Abstract*—Predictive and reliable models are key tools for the development of the next generations of single photon avalanche diodes (SPADs). Models are indeed crucial to evaluate the performance of prospective detector structures and to down select the most promising solutions before developing and running a dedicated fabrication process. To ensure predictability, models must be extensively validated against experimental data. In particular, the model must be applied to existing detectors and the results obtained from simulations must be compared with the measurements performed on the same detectors. The ability to accurately extract the doping profile along the SPAD active region plays a crucial role in the validation flow, because SPAD properties generally exhibit a strong dependence on the electric field. In this article we will discuss why widely-adopted doping profile techniques do not allow the calculation of the electric field with an accuracy sufficient for predictive SPAD modeling. Then, we will present a technique we developed to extract accurate doping profiles starting from an approximate device-structure built with process simulations and/or secondary ion mass spectroscopy (SIMS) measurements. The technique combines capacitance-vs-voltage measurements with device simulations to implement an inverse modeling scheme. Finally, we will show how the proposed technique allows us to accurately reproduce the breakdown voltage of a large set of SPADs.**

***Index Terms*—Breakdown voltage simulation, doping profile extraction, inverse modeling, single photon avalanche diode (SPAD), SPAD modeling.**

I. Introduction

SINGLE photon avalanche diodes (SPADs) are solid-state devices that exploit self-sustained avalanche multiplication in a semiconductor junction to reveal the arrival of a single photon [1]. They are widely used in an ever-growing number of applications that span from fundamental research to consumer electronics. For example, SPADs are employed: in medical imaging, to measure tissues' properties by means of non-invasive techniques like diffuse optical tomography (DOT) [2]; in autonomous driving, to create real-time three-dimensional maps of the environment by exploiting light detection and ranging (LiDAR) [3]; in communications, to ensure secure data exchanges through quantum key distribution (QKD) [4]; in biochemistry, to reconstruct the properties of a heterogeneous population of molecules by analyzing fluorescence intensity and lifetime [5].

A. Recent Progresses and Challenges

The wide diffusion of SPADs in so many applications has been fostered by a combination of good performance, affordability, and easiness of use. On the one hand, SPADs for visible and near infrared wavelengths are silicon devices, with all the advantages that follow: operation at room temperature or moderately cooled (e.g. -10 °C), large volume production at low cost, robustness, compactness, and scalability. On the other hand, new SPAD designs introduced in the last decade have allowed to reach remarkable performance in specific domains. For example, charge focusing structures [6], [7] enable high fill-factor arrays with a detection efficiency extended into the infrared; red-enhanced SPADs (RE-SPAD) by Gulinatti et al. [8] combine low timing jitter with high detection efficiency at red and near infrared wavelengths; SPADs fabricated in a customized BCD (bipolar, CMOS, and double-diffused MOS) technology by Sanzaro et al. [9] provide an ultra-clean temporal response with high detection efficiency at visible wavelengths; SPADs developed by Pratte et al. [10] and by Gramuglia et al. [11] attain an ultra-low timing jitter.

These examples clearly show the potential of adopting new detector structures and new designs in improving specific SPAD metrics. They highlight also that SPAD metrics are subjected to multiple trade-offs so that an improvement in a certain parameter usually leads to a degradation in other figures of merit. However, innovative structures and clever designs can push farther the boundaries set by performance trade-offs.

Despite the incredible steps forward of the last decade, a lot of work is still necessary to address the needs of a variety of applications whose potential cannot be fully exploited with currently available detectors. For example, RE-SPADs provide a combination of high detection efficiency and low timing jitter which is almost ideal for single-molecule analysis. They can be arranged in arrays, but the spacing between the pixels must be large (e.g. 250 μm) [12] because of the bulky guard rings that surround the device. This is sufficient for high-throughput single-molecule analysis of freely diffusing molecules [13],

Manuscript received 30 April 2023; revised 15 August 2023 and 28 November 2023; accepted 5 December 2023. Date of publication 11 December 2023; date of current version 2 January 2024. This work was supported by the Human Frontier Science Program (HFSP) under Grant RGP0061/2019. Red-enhanced SPAD were fabricated by some of the authors at the Cornell NanoScale Facility, a member of the National Nanotechnology Coordinated Infrastructure (NNCI), which was supported by the National Science Foundation under Grant NNCI-2025233. *(Corresponding author: Angelo Gulinatti.)*

The authors are with the Dipartimento di Elettronica, Informazione e Bioingegneria, Politecnico di Milano, 20133 Milan, Italy (e-mail: andrea.bonzi@polimi.it; gabriele.laita@polimi.it; ivan.rech@polimi.it; angelo.gulinatti@polimi.it).

Color versions of one or more figures in this article are available at https://doi.org/10.1109/JSTQE.2023.3341349.

Digital Object Identifier 10.1109/JSTQE.2023.3341349

© 2023 The Authors. This work is licensed under a Creative Commons Attribution 4.0 License. For more information, see https://creativecommons.org/licenses/by/4.0/

where a few tens of largely spaced detectors acquire the fluorescence signal in as many independent spots. However, for fast kinetic studies, single molecules are flowed along a microfluidic channel [14] and a linear array of hundreds of closely packed SPADs is essential to follow the evolution of the population in time. As another example, high-rate QKD through satellite links [15], [16] requires a combination of ultra-clean temporal response and high PDE at 850 nm [17] that neither RE-SPADs presented in [8] nor BCD SPADs described in [9] can currently provide. Even more challenging are the requirements for optical quantum computing [18], where a photon detection efficiency (PDE) largely exceeding 90% must be attained in combination with scalability and with low coupling losses with photonic circuits.

B. Technology Options

Two factors play a key role for developing SPADs that can overcome the current trade-offs and satisfy the requirements of the most challenging applications: the possibility of freely designing each part of the detector's structure, and the availability of accurate models that allow to understand and evaluate the impact of each modification on relevant SPAD metrics. Regarding the first point, the degree to which the detector structure can be changed, strictly depends on the technology adopted for its fabrication. With standard CMOS or BCD technologies, the designer can only choose how to combine a set of predefined regions (e.g. shallow diffusions, deep wells, etc.) made available in the selected process flow. Despite this limited freedom, a proper detector design can still have a dramatic impact on detector performance; for example, the introduction of a p-type layer in [19] compared to [20] allowed to significantly trade short-wavelength detection efficiency for a faster temporal response.

A slightly higher design freedom can be obtained with the support of the foundry that runs the fabrication process. In this case, it is possible for example to add one or more ion implantations to tailor the doping profile in certain regions. This approach has been adopted for example by Sanzaro et al. in [9], who introduced custom high-energy phosphorus and boron implants to create a deep-junction SPAD. However, it should be noted that the modifications to the process flow cannot include for example additional thermal treatments that would otherwise impact the doping profile in other regions.

The highest degrees of freedom are attained by resorting to a custom technology, i.e. a process flow specifically designed for the fabrication of the detector (rather than for transistors). In this case the designer can choose and optimize each step of the fabrication to attain the desired structure. The obvious drawback of this approach is the absence of transistors integrated on the same chip of the detector. The electronic circuitry needed to drive and readout the detector must therefore be fabricated on a different chip and connected to the detectors either through wire-bonding [21] or 3D stacking [22]. A remarkable example of the potential provided by the combined use of custom technologies with 3D stacking can be observed with SPAD arrays for LiDAR. Researchers at Sony Semiconductor have developed a few generations [23], [24], [25] of back-illuminated, 3D-stacked SPAD arrays that attained impressive performance in terms of PDE at 940 nm, timing jitter, and pixel density. These results have been made possible thanks to a thick absorption layer, a metal back reflector, and a suitable engineering of the electric field. When such degrees of freedom are not available, performance are inevitably lower [26], [27].

C. Models: Role and Challenges

Whatever is the approach adopted for the fabrication of the detector, models able to accurately forecast detectors' performance play a crucial role for the evolution of SPAD technology (see [28] for a general review on available SPAD models). Models not only allow to optimize the design for a specific application, but, even more importantly, they allow also to investigate multiple design trade-offs and to evaluate the effectiveness of new structures before performing a full fabrication. This is especially important for custom technologies in which the development of a new process is particularly expensive and time-consuming. Therefore, the ability to select in advance only the most promising solutions and to minimize the number of iterations needed to obtain an optimized detector is especially welcomed.

The design of a new detector can, in part, be tackled by fabricating a large set of SPADs with different layouts (called a SPAD farm) and by selecting the one with the best performance metrics as resulting from a full experimental characterization. Although this pragmatic approach has gained some popularity, especially with CMOS technologies [29], it does not supersede the need of predictive models. SPAD farms do not provide an insight in detector physics, and they are a viable option only to explore layout variations (rather than process variations).

The development of models which are more and more accurate and reliable requires a thorough and extensive validation against experimental data. Measurements performed on different SPADs must be compared with the results generated by the models. A common limiting factor in this process is the poor knowledge of the electric field profile of measured SPADs. In fact, on the one hand, most of the physical processes involved in SPADs' operation present a strong, exponential-like dependence on the electric field; among them are for example impact ionization [30], band-to-band tunneling [31], and field-enhanced emission of carriers from localized energy levels [32]. These processes play a key role in determining SPADs properties like breakdown voltage, PDE, dark count rate (DCR), timing jitter, and afterpulsing probability. Consequently, a predictive and accurate modeling of SPAD performance requires a precise knowledge of the electric field along the detector. On the other hand, the electric field profile in a detector cannot be measured directly; it must be rather calculated from the doping profile by solving the Poisson equation with appropriate boundary conditions. Unfortunately, as will be discussed in the following sections, the techniques commonly used to measure the doping profiles in semiconductor devices provide results which are not accurate enough for SPAD modeling.

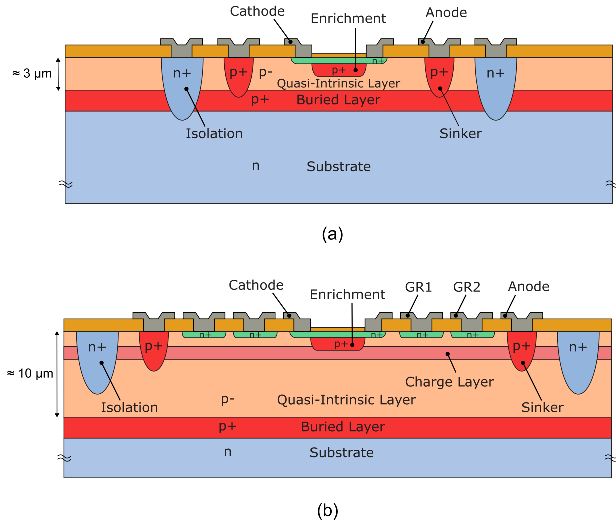

Fig. 1. Cross section of a thin SPAD (a) and of a Red-Enhanced SPAD (b).

D. This Work

To overcome this limitation, in this paper we will present an inverse modeling approach which relies on the combined use of electrical simulations and capacitance-voltage (C-V) measurements. A commercial technology computer-aided design (TCAD) software is exploited to build a model of the device under test and to simulate its capacitance versus voltage curve. The simulated C-V curve is compared with the experimental one, then the doping profile of the model SPAD is adjusted until the simulated result matches the experimental data.

The paper is organized as follows. After providing in Section II a brief introduction on the SPAD structures used in this work, in Section III we will discuss why conventional doping-profile techniques are not accurate enough for SPAD modeling. In Section IV we will introduce the proposed inverse modeling method, of which we will provide a numerical and an experimental validation respectively in Sections V and VI. Finally, in Section VII we will discuss the obtained results and we will draw some conclusions.

II. Thin and Red-Enhanced SPADs

For the description and the validation of the inverse doping profile method presented in this paper, we will refer to two specific SPAD structures developed in our laboratories, namely thin SPAD and red enhanced SPAD (RE-SPAD). For the sake of clarity, in this section we will provide a brief overview of their structure and properties. However, it should be noted that the method presented in this paper is not limited to these detectors and can be extended to other structures.

The typical structure of a double epitaxial thin SPAD developed at Politecnico di Milano [33] is shown in Fig. 1(a). The device is fabricated starting from an n-type substrate on top of which has been grown a p-type epitaxial layer, composed by a p+ *buried layer* and a p- *quasi-intrinsic layer*. During the subsequent fabrication steps, the following regions are manufactured: *shallow n*, a thin phosphorus diffusion that constitutes the cathode of the device; *enrichment*, a medium thickness p+ region that confines the avalanche process in the central part of the detector thus avoiding premature edge breakdown; *sinker*, a deep p+ region that complements the role of the buried layer in providing a low-resistance path from the SPAD active area to the anode contact; *isolation*, a deep n+ region which forms with the substrate a pocket that entirely surrounds the device and electrically isolates it from the adjacent pixels.

The relatively small thickness of the quasi-intrinsic layer (typically 2 - 3 μm) limits the PDE at red and near infrared wavelengths. The PDE reaches a maximum of about 50% at 550 nm and drops to 15% at 800 nm. However, the thin absorption layer results in a sharp temporal response with a timing jitter as low as 35 ps FWHM [34], [35].

To overcome the limitations of thin SPADs in terms of detection efficiency, some of the authors developed the so-called red-enhanced SPAD (Fig. 1(b)) [8]. RE-SPADs are characterized by a thicker quasi-intrinsic layer ($\approx$ 10 μm), which ensures a higher absorption efficiency for red and near-infrared photons. An additional p-type epitaxial layer, indicated as *charge layer*, has been introduced below the enrichment, at the edge of the multiplication region. This layer plays a key role in shaping the electric field to optimize parameters like the breakdown voltage, the timing jitter, and the DCR. Edge breakdown, which is more severe in thick SPADs, is prevented by resorting to *guard rings* that surround the cathode region. This class of detectors is capable of attaining a PDE similar to thick SPADs [36] in the near infrared range (e.g. 40% at 800 nm), while maintaining a remarkable timing jitter of about 90 ps FWHM [37].

III. Conventional Doping Profiling Techniques

In this section we will briefly discuss different techniques commonly employed for determining the doping profile. We will highlight their strengths and weaknesses, and we will focus on the reasons why their level of accuracy and precision is not high enough to correctly predict SPADs performance.

A. Process Simulation

TCAD software includes multiple packages conceived to design and optimize semiconductor devices. Among them, there are the so-called process simulators, i.e. software that are able to calculate the structure of a semiconductor device starting from a description of its fabrication process. The dopants distribution and the device topography are obtained by solving the equations that describe the physical processes that happen during the manufacturing (e.g. diffusion, oxidation, etc.). Therefore, process simulation can be regarded as an interesting option to obtain the doping profile of a SPAD, if the details of the fabrication process are known.

Today, process simulators include highly sophisticated models which are calibrated with data from equipment vendors, and which are continuously improved and optimized to increase their accuracy and to extend their range of validity. Nevertheless, a custom calibration is usually needed to reproduce the behavior of a given technology with a high degree of accuracy. This procedure, which consists in fine-tuning some models' parameters such that the simulated profiles match the experimental ones, is needed to account for the limited accuracy of the models,

non-idealities in manufacturing tools, unmodeled process interactions, etc.

Process simulations are therefore extremely useful to attain the general structure and first-order doping distributions in a device. However, they must be complemented with some techniques that allow a precise and accurate measurement of the doping profile in manufactured samples. Such measurements can be either used to refine the knowledge of the doping profile in the most critical regions of the device or to perform a custom calibration of the simulator. Doping profile measurements are also needed to understand and address non-uniformities that typically affect real fabrication processes and that can be hardly accounted for in process simulators.

B. Secondary Ion Mass Spectrometry

Secondary ion mass spectroscopy (SIMS) can be regarded as the gold standard for measuring doping profiles in semiconductor technology [38]. The technique relies on the removal of material from the sample by physical sputtering and on the collection and analysis of the sputtered ionized atoms through a mass spectrometer.

The main advantages of SIMS for doping profiling are the high depth resolution (down to 1 nm), and the excellent dynamic range (up to 6 orders of magnitude). On the other side, SIMS is plagued by some limitations: it determines the total dopant density rather than electrically active concentration (the two might differ in case of partial activation of the dopant); it requires a complex and expensive equipment, along with sophisticated calibration procedures; it is a destructive method, as the physical act of removing material by sputtering leaves a crater in the sample; it suffers of poor accuracy and sensitivity at low and medium doping concentrations; the profiles might be affected also by the accuracy in the estimation of silicon surface position and crater depth.

Because of its peculiarities, SIMS is routinely used to measure the doping profile in many regions of a variety of semiconductor devices (e.g. shallow junctions, deep wells, etc.). However, it is not suitable for every purpose. In particular, SIMS is not the ideal technique when a medium or low doped region needs to be characterized with high accuracy and precision. This is exactly the case of the enrichment and charge-layer regions in a SPAD detector.

To better illustrate this point, we report an example of an investigation we performed to troubleshoot some process non-uniformities. In particular, we wanted to investigate the variation of the breakdown voltage across a wafer containing RE-SPADs. So we had the doping profile of three detectors - namely A, B, and C - measured by SIMS technique in a highly qualified laboratory. The three detectors are taken from the same wafer and are nominally identical. However, they present different breakdown voltages, respectively of 80.7, 71.6, and 63.7 V. In a structure as in Fig. 1(b), the higher is the enrichment dose, the lower is the breakdown voltage, so we would have expected an increase of the dose moving from device A to C. However, by calculating the enrichment dose from the SIMS profiles, we observed an increase of 5.1% moving from device A to B, but a reduction of 3.4% from device B to C. This non-monotonic behavior of the enrichment dose is clearly incompatible with the measured breakdown voltages and can be attributed to the limited precision of SIMS techniques in assessing doses in the order of some 10^{13} atoms/cm^{-2}, as those typically present in a SPAD multiplication region. The problem is strictly related to the strong dependence of the breakdown voltage on the enrichment dose. For example, for a typical sizing of the structure in Fig. 1(b), simulations allow us to assess that a variation of 1% in the enrichment dose can result in a breakdown change as high as a few volts.

C. Capacitance-Voltage

The weaknesses of SIMS measurements can be addressed by complementing SIMS profiling with alternative techniques. Among them, the most widely used is the capacitance-vs-voltage (C-V) profiling [38].

This technique can be adopted when a depletion region is available and its extension can be modulated by changing the applied voltage, as it happens for example with pn junctions, Schottky barrier diodes, and MOS capacitors. The method exploits the dependence of the small-signal capacitance $C = dQ/dV$ on the doping concentration $N(x_d)$ at the edge x_d of the depletion layer. In fact, when the applied voltage is increased of an amount dV, the space charge region expands on an amount dx_d, and a charge $dQ = qN(x_d)dx_d$ is removed at its edge. From this relation it is clear that dQ, and hence C, contains information on the doping concentration in x_d; if the edge of the space charge region is swept across the device by progressively increasing the voltage V, the doping profile can be attained by resorting to the following equations [38]:

$$N(W) = \frac{2}{q \cdot \varepsilon_r \cdot \varepsilon_0 \cdot A^2 \cdot \frac{d(1/C^2)}{dV}} \quad (1)$$

$$W = \frac{\varepsilon_r \cdot \varepsilon_0 \cdot A}{C} \quad (2)$$

where N is the doping concentration, W and A respectively the extension and the area of the depletion layer, C the differential capacitance, V the applied DC voltage, q the electron charge, and $\varepsilon_r \cdot \varepsilon_0$ the permittivity of the semiconductor material.

C-V profiling has some distinctive advantages over SIMS: it provides better sensitivity at lower doping concentrations, is non-destructive, and can be easily and quickly performed with LCR meters, which are relatively inexpensive and available in most electronics laboratories. These properties make C-V profiling appealing not only to complement SIMS data in lowly doped regions, but also to carry our additional investigations. For example, differently from SIMS, C-V measurements can be easily performed on a large number of devices across a wafer to elucidate the causes of process non-uniformities. However, C-V profiling is also affected by some limitations. For example, differently from SIMS, C-V can only probe the doping concentration at the edge of a depleted region. This means that the doping profile near the junction cannot be extracted due to the extension of the zero-bias space-charge region; similarly, an upper limit to the probing depth is set by the breakdown voltage. Also, the C-V method returns the doping concentration as a function of the space charge width, see (1), rather than as a function of the distance from the silicon surface. These aspects

are especially critical for SPAD modeling because they prevent a direct calculation of the electric field profile from the results of a C-V measurement.

Even more importantly, (1) and (2) have been derived under the assumption of charge neutrality, depletion approximation, and unilateral one-dimensional junction. Not complying entirely with these assumptions might have an adverse effect on the extracted doping profile; this issue has been extensively investigated in literature [39], [40], [41], [42], [43], [44], [45]. For the sake of convenience, the main results will be summarized in the following. Firstly, charge neutrality assumes that the carrier concentration is equal to the dopant concentration in each point of the detector outside the depleted region. However, when a dopant gradient is present, carriers diffuse from the regions with a higher concentration to those with a lower concentration, leaving behind partially uncompensated dopants in the former region and generating excess carriers' accumulation in the latter. An equilibrium is eventually reached when the electric field generated by charge-unbalance compensates the diffusion process. Kennedy et al. [40] concluded that, in this case, (1) should be replaced by:

$$c(W) = \frac{2}{q \cdot \varepsilon_r \cdot \varepsilon_0 \cdot A^2 \cdot \frac{d(1/C^2)}{dV}} \tag{3}$$

where $c(W)$ is the majority carriers' concentration. Therefore, the C-V technique allows to retrieve the majority carriers' concentration rather than the doping concentration that would be needed for the calculation of the electric field. The two concentrations may differ more or less significantly depending on the specific doping profile. Secondly, the so-called depletion approximation assumes the existence of a sharp boundary between the depletion layer and the quasi-neutral layer, such that the carriers' concentration on one side of the boundary is zero and abruptly rises to the equilibrium value on the other side. Actually, the transition is smoother and happens on a distance of a few Debye lengths. Johnson and Panousis [46] showed numerically that the resulting effect is an averaging of the extracted profile on a distance comparable with the local Debye length. Therefore, the C-V technique may not be able to resolve sharp transitions, especially at small dopant concentrations where the Debye length is relatively large. Thirdly, if the junction is not strongly asymmetrical, the depletion layer expands on both sides of the junction as the voltage is increased. Consequently, the value returned by (3) is a combination of the carriers' concentration at the two boundaries of the depletion layer. Many solutions have been proposed to account for this issue, but no one can be easily applied. Finally, if edge effects and parasitic contributions affect the value of the measured capacitance, the extracted doping profile can be distorted significantly. An example of this effect will be provided in Section V.

IV. Inverse Doping Profiling

In the previous section we highlighted that the C-V technique is potentially very interesting because of its sensitivity, inexpensiveness, and non-destructiveness. However, it can be rarely used to directly extract the doping profile in a SPAD because the extraction procedure relies on hypotheses which are hardly satisfied in real detectors.

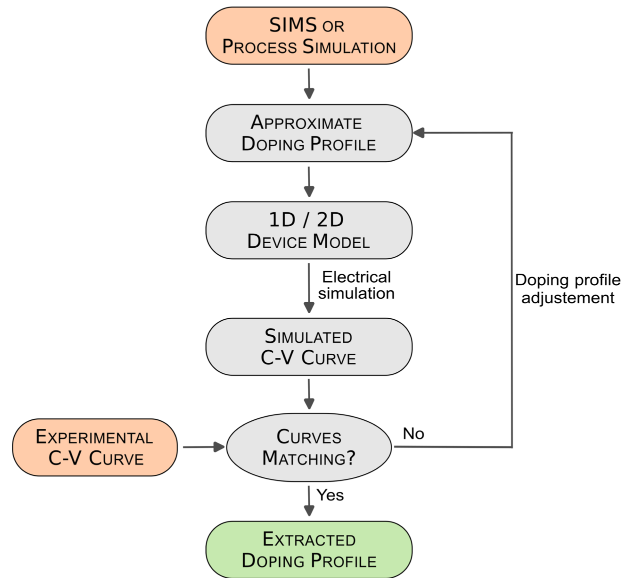

Fig. 2. Flowchart illustrating the proposed doping extraction technique: the doping profile in a SPAD-model is adjusted until the simulated C-V curve matches the experimental data; the initial guess is generated starting from SIMS and/or process simulations.

To benefit of the advantages of the C-V technique without suffering of the limitations of the direct extraction procedure, we adopted the inverse approach illustrated in Fig. 2. The approximate doping profile obtained either from SIMS or from process simulations is used as a starting point to build a numerical model of the device under test (DUT). A C-V curve is calculated from the model (through a device simulator) and is compared with the one obtained experimentally from the DUT. Assuming that any difference between the two curves can be ascribed to a mismatch between the doping profile in the model and in the real device, the former doping profile is modified until a perfect match between the experimental and the simulated C-V curve is obtained.

The inverse approach of Fig. 2, also known as inverse modeling [47], does not suffer of the limitations of the direct extraction because non-idealities (e.g. edge effects, carriers diffusion, etc.) can be accounted for in the model. So, provided that the model is an accurate description of the DUT, the simulated C-V curve matches the experimental one when the doping profile in the model corresponds exactly to the one in the real device. The doping profile in the model represents therefore the outcome of the extraction process.

The use of inverse modeling to assess the doping profile of certain semiconductor devices from C-V measurements have already been presented in literature. For example, Khalil et al. [48], [49] have successfully applied the method to determine the two-dimensional doping profile of a submicron MOSFET. However, the implementation of an inverse modeling is strictly related to the type of device and to its structure.

In the following sub-sections we will describe how we apply the inverse modeling to extract the doping profile of a one-dimensional and a two-dimensional SPAD; then we will briefly

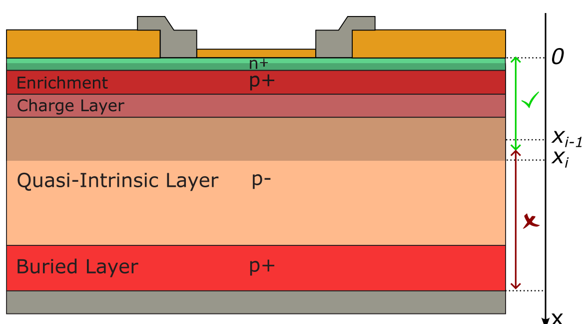

Fig. 3. 1-D SPAD structure, corresponding to the central region of the device depicted in Fig. 1(b). The shaded area indicates the extension of the space charge region at the i-th step of the extraction procedure. The green and red arrows indicate respectively the regions where the doping profile has been and has not been already corrected.

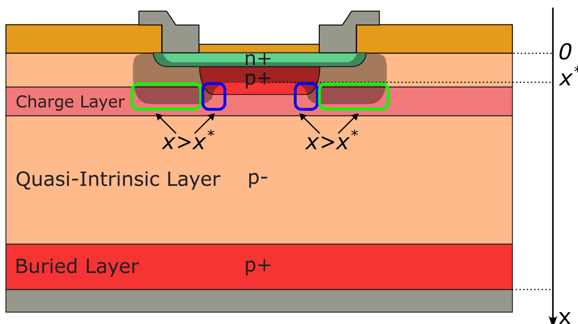

Fig. 4. 2-D SPAD structure. The shaded area indicates the extension of the space charge region (SCR) when a certain voltage V^* is applied. x^* is the SCR depth in center of the device. Green and blue boxes highlight the regions where the SCR extends beyond x^*.

comment on our implementation and on how it compares to other examples reported in literature.

A. One-Dimensional SPAD Structure

For the sake of simplicity, we start by illustrating our method on the one-dimensional SPAD structure depicted in Fig. 3.

We assume that a reasonably good estimate of the doping profile along the detector is available either from SIMS or process simulation. The aim of the method is to refine the knowledge of the boron profile in the region that spans from the np junction to the upper boundary of the buried layer. The doping profile of this region is especially important because it determines the electric field in the detector.

To sweep the region of interest with the lower edge of the depleted region, the reverse voltage applied to the structure is progressively increased from a minimum value V_{MIN} close to zero to a maximum value V_{MAX} slightly below the breakdown voltage. Let's indicate with V_i the voltage applied at the $i-$th step of the procedure, x_i the lower boundary of the depleted region, $C_{meas,i}$ and $C_{sim,i}$ respectively the value of measured and simulated capacitance. If the simulated capacitance matches the measured capacitance in all the previous steps (i.e. from 0 to $i-1$), then we can assume that the boron profile $N_B(x)$ is correct from the junction down to x_{i-1}, and that an error $\Delta C_i = C_{meas,i} - C_{sim,i}$ would be exclusively due to a mismatch in the doping concentration around x_i. In such case, the boron concentration $N_B(x = x_i)$ can be modified until the error ΔC_i vanishes, and the procedure can move on to the next step (i.e. step $i+1$).

Regarding the adjustment of the doping concentration around x_i, an iterative approach is adopted in which $N_B(x = x_i)$ is changed until the capacitance error drops below a preset tolerance. At each step of the iteration, $N_B(x = x_i)$ is either decreased or increased of a percentage ε^- or ε^+ respectively if the simulated capacitance exceeds or falls behind the measured one:

$$N_B(x_i) = \begin{cases} N_B(x_i) \cdot (1-\varepsilon^-), & \text{if } C_{sim,i} > C_{meas,i} \\ N_B(x_i) \cdot (1+\varepsilon^+), & \text{if } C_{sim,i} < C_{meas,i} \end{cases} \quad (4)$$

Such procedure is justified by the fact that a larger (smaller) doping concentration results in a narrower (wider) space-charge region and consequently in a higher (lower) capacitance value.

Actually, at each step, the aforementioned correction is applied for every $x \geq x_i$, rather than only in $x = x_i$. This strategy is suggested by the fact that the doping profiles are continuous and slowly varying. So, for example, if the doping concentration has been underestimated in x_i, there is a good chance that it has been underestimated also in the region right beneath x_i. If this is not the case, the error is fixed anyway in the following steps. However, this approach usually accelerates the convergence of the algorithm in the following steps.

B. Two-Dimensional SPAD Structure

Many of the test structures used for C-V measurements have non-negligible edge effects. To account for them properly, the simulations and the iterative doping adjustment must be performed on a two-dimensional model.

To illustrate how the extraction method is implemented in the two-dimensional case, we will refer to the structure of Fig. 4. Depending on the thickness of different layers and on the presence or absence of the charge layer, such a structure can represent either a thin or a red-enhanced SPAD. In both cases, to a first instance, the p-type area can be divided into two regions characterized by different boron profiles: a *central region* in which the boron profile $N_{B,center}(x)$ includes the enrichment implantation, and a *lateral region* whose boron profile $N_{B,lateral}(x)$ does not.

The shaded area of Fig. 4 represents the space charge region when a certain voltage V^* is applied to the device. As the space charge extends beyond the central region, ΔC can be due to an error in the doping concentration either in the central or in the lateral region. That raises the question of how to adjust the doping profile to extinguish ΔC (i.e. by adjusting $N_{B,center}$, $N_{B,lateral}$, or both). To address this problem, we can split the extraction procedure in two phases.

Let's initially assume to know exactly the doping concentration $N_{B,lateral}$ in the lateral region. In this case, for any applied voltage V^*, the corresponding error $\Delta C(V^*)$ can be ascribed only to the central region of the device. Thereby, the doping

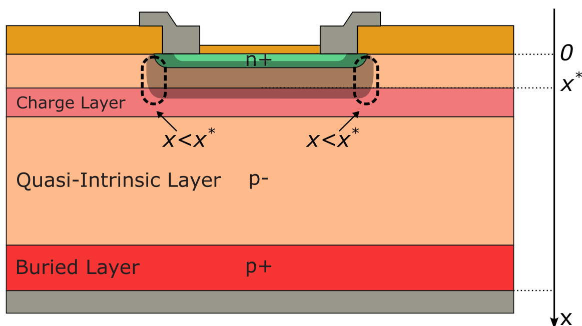

Fig. 5. 2-D SPAD structure without the enrichment. The shaded area indicates the extension of the space charge region (SCR) when a certain voltage V^* is applied. x^* is the SCR depth in center of the device. The dashed boxes highlight that the SCR in this case do not extend beyond x^*.

concentration in central region, $N_{B,center}$, can be adjusted following the same procedure outlined in the previous sub-section (i.e. by progressively increasing the bias voltage V from V_{MIN} to V_{MAX}). However, before performing the correction in central region, we must determine accurately the doping profile in the lateral region. To this purpose we can resort to the structure represented in Fig. 5, which is identical to the one in Fig. 4 except for the absence of the enrichment. As in this structure the boron profile is uniform across the device and equal to $N_{B,lateral}$, the correction can be performed again as in the 1D case. In summary, the extraction procedure requires the availability of the two structures of Figs. 4 and 5. The one without the enrichment is used in the initial phase to attain the lateral profile $N_{B,lateral}(x)$. This profile is mandatory to build a good model of the structure with the enrichment, which is then used in a second phase to extract $N_{B,center}(x)$. It's worth noting that the fabrication of the structure of Fig. 5 requires only a minimal modification in the SPAD layout, consisting in removing the enrichment mask from the detector area.

The approach adopted for the two-dimensional structures deserves some additional comments:

1) The procedure outlined above assumes the knowledge of the doping profile in the cathode region. Since SIMS measurements provide only 1D profiles, the 2D doping profile at the edge of the cathode can be either assessed with process simulations or built analytically by convolving the vertical SIMS profile with a lateral roll-off function (e.g. Gaussian). Multiple simulations allowed us to conclude that the shape and the width of the transition have a negligible effect on the calculated capacitance and on the extracted boron profile.
2) When a voltage V^* is applied to the structure of Fig. 5 the depth of the depletion region reaches its maximum x^* in the center, while it is smaller at the edges. Therefore, the capacitance depends not only on the boron concentration in x^*, but also in $x < x^*$. However, as the boron concentration in $x < x^*$ has already been corrected in the previous steps, we can assume that the error is entirely due to the doping concentration in x^*; hence, the correct doping profile is again obtained by adjusting $N_B(x^*)$ until ΔC vanishes.
3) We previously assumed that the boron-doped region can be sharply separated in a central and a lateral region. However, during high temperature processing steps, the boron in the enrichment diffuses laterally, so there is a smooth transition between the two regions. The lateral shape of the enrichment profile can be modeled with the same approach adopted for the cathode. Simulation results allowed us to conclude that the shape and the extension of this transition region plays only a minor role in determining the value of the capacitance. Consequently, for the sake of simplifying the implementation, we perform the doping extraction assuming an abrupt transition between the regions.
4) Differently from the case in Fig. 5, when a voltage V^* is applied to the structure of Fig. 4, in some regions the depletion layer extends also beyond x^*. Consequently, the capacitance $C(V^*)$ will depend also on the boron concentration at $x > x^*$. This is not an issue for the lateral regions indicated by the green boxes in Fig. 4. In fact, in these regions the doping profile has already been corrected during the first phase of the extraction, so they do not contribute to the capacitance error. However, the depleted layer expands beyond x^* also at the edges of central region (see shaded areas indicated by the blue boxes in Fig. 4). Here the doping profile is $N_{B,center}$ which is still not corrected for $x > x^*$. As the correction algorithm tries to zero ΔC by changing only the doping profile at $x = x^*$, this may lead to an error in $N_{B,center}(x = x^*)$. This problem is dealt with by repeating multiple times the second phase of the correction procedure. Every time this phase is iterated, the boron profile in $x > x^*$ is closer to the correct profile, so the correction in $x = x^*$ is performed with better data and the error in $x = x^*$ reduces as well at each iteration (provided that the initial guess is good enough).

C. Implementation

The method described in this paper has been implemented by using a combination of Matlab and of the TCAD suite Sentaurus by Synopsys. In particular, given a certain device structure (i.e. a 1D or 2D doping distribution) and a set of applied voltages, the device simulator Sentaurus Device solves the semiconductor equations and calculates the relevant electrical properties. Then, the C-V curve and the boundaries of the space charge region are calculated and exported by using Sentaurus Visual, a tool designed to elaborate and plot the results produced by the TCAD tools. The exported data are analyzed in a Matlab script, which calculates the updated doping profile on the basis of the comparison between the experimental and the simulated C-V curves. Finally, the new profiles are fed to Sentaurus Process to build the device structure for the next iteration. Beside calculating the updated profiles, the role of the Matlab script is to automate the execution of the algorithm by running the right sequence of tools with the proper inputs. The typical running time on a desktop computer ranges from about 10 minutes for a 1D structure to some hours for a large 2D device.

Compared to most of the works previously reported in literature, the method presented in this paper differs in some respects. Firstly, in many inverse schemes (see for example [50] and [51]) the doping profile is described by some analytical functions and their parameters are adjusted to minimize the error. Although simple, this solution is not well-suited to reproduce accurately real doping profiles, the shape of which is affected by second-order effects. Secondly, even in those cases in which the doping profile has been discretized over a suitable mesh, a different approach has been used to find the solution. For example, Khalil et al. [52] use a global approach in which the doping concentration in each point is changed simultaneously to minimize the overall distance between the experimental and the simulated C-V curve. By contrast, in this paper a local approach has been adopted in which, for each voltage V^*, only the doping concentration at the edge of the space charge region is modified to minimize the error on $C(V^*)$. This solution allows to reduce the computational complexity and to work with much larger meshes for a better description of the doping profile and of the edge effects.

V. Numerical Validation

The effectiveness of the inverse method described in the previous section can be verified by showing that the iterative scheme converges to the correct solution when starting from an incorrect doping profile. As in real devices the doping profile is not precisely known, it is preferable to perform this validation on a simulated structure, the doping profile of which is perfectly known. As a first step, the C-V curve of such a reference structure is obtained by numerical simulation. Then a new structure, with a slightly different boron profile, is considered. The iterative method is applied to the new structure, which will be called *test structure*, until its C-V curve matches the one of the reference device. The extracted doping profile is then compared with the reference profile to verify its correspondence. In this section we will apply this procedure to a 1D and a 2D case to show the effectiveness of the inverse method. Moreover, a comparison with a direct doping extraction from C-V measurements will be done in order to highlight how all the limitations of the classical method are overcome with our procedure.

A. One-Dimensional SPAD Structure

The procedure outlined above has been initially applied to the one-dimensional structure depicted in Fig. 3.

The gray curve in Fig. 6(a) represents the boron profile in the reference structure, while the green curve the initial guess in the test structure. The initial guess differs from the reference doping profile in two aspects: the enrichment dose is 15% lower, and the intrinsic layer is about 500 nm thinner (so the buried layer is closer to the enrichment). The red curve represents the extracted profile obtained by applying the iterative method on the test structure. From Fig. 6(a) it is clear that the iterative method succeeds in correcting both the types of error in the initial guess, leading to an extracted profile that closely matches the reference profile. The only notable differences are a few steps of non-negligible amplitude in the region where the boron concentration approaches its minimum value. The presence of

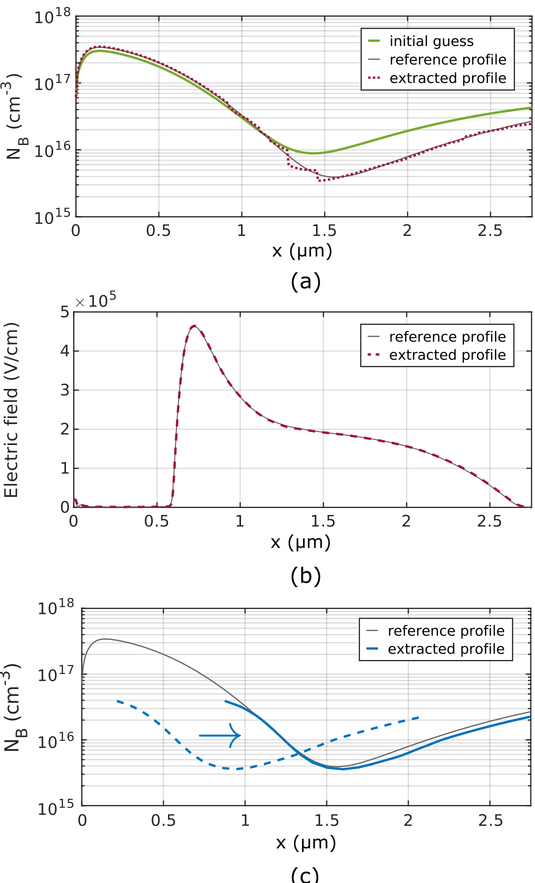

Fig. 6. (a) Inverse doping profiling procedure applied to the 1D structure of Fig. 3. Gray, green, and red curves represent respectively the reference profile, the initial guess, and the result of the extraction procedure. (b) Comparison between the electric fields calculated from the reference (gray) and the extracted (red) doping profiles. (c) Doping concentration obtained with a direct extraction, i.e. by applying (1) and (2) to the C-V data. An acceptable matching between the reference profile (gray) and the extracted data (dashed-blue) is obtained only after the curve has been shifted (solid blue) of an amount which is not known in real measurements.

these steps can be explained by considering the procedure with which the doping profile is adjusted. For a certain voltage V^*, the correction algorithm changes the doping profile of a factor ϵ (see (4)) for each $x > x^*$, thereby introducing a step in the doping concentration. As the correction is repeated until the error ΔC falls below a certain threshold, the amplitude of these steps is usually very small. However, in the considered region, the C-V curve presents a weak dependence on the doping profile. Therefore, the error can fall below the threshold even when the mismatch between the extracted and the reference doping profile is not so small.

While it could be possible to reduce the steps amplitude by reducing the preset error-threshold and the voltage step in the C-V measurement, this is typically not necessary. Indeed, the electric field profile, which is the quantity of real interest for SPADs simulations, has in turn a weak dependence on the doping concentration in the same region. This concept is exemplified in Fig. 6(b), in which the electric fields attained from the reference and the extracted profile are compared. From the figure it is clear that no significant differences between the

electric fields are present despite the residual errors in the low doping concentration region.

For the sake of comparison, Fig. 6(c) reports the profile obtained by using a direct extraction from the C-V curve. As (1) and (2) provide the doping concentration as a function of the depleted layer extension, rather than from the silicon surface, the resulting curve has been translated of a suitable amount to allow a comparison with the reference doping profile. While the matching is good in the central region, some notable errors are present for $x < 1$ μm and for $x > 1.6$ μm. Even more important, the results obtained from the direct extraction are of small practical use for SPAD modeling. In fact, the lack of information on the doping profile close to the junction and the need for translation of an amount which is not precisely known prevent the calculation of the electric field profile. Conversely, as clear from Fig. 6(b), the calculation of the electric field is straightforward with the information provided by the inverse method.

B. Two-Dimensional SPAD Structure

The same validation scheme has been applied to a two-dimensional structure such the one depicted in Fig. 4. The simulated structure has an active area diameter of 50 μm. The reference boron profile in the lateral and in the central regions are represented in gray respectively in Fig. 7(a) and (b). A two-phase procedure like the one described in Section IV-B has been applied to extract the lateral boron profile first, and then the central boron profile. As in the one-dimensional case, the initial guess for the boron profile has an enrichment dose 15% lower than in the reference profile and an intrinsic layer which is 500 nm thinner.

During the first phase, a test structure without the enrichment region (such the one depicted in Fig. 5) has been used to extract the lateral profile $N_{B,lateral}$. Fig. 7(a) represents in green the initial guess, and in red the lateral profile extracted by using the inverse method. The correspondence between the reference and extracted profile is good, apart the small steps discussed earlier. The extracted lateral profile has then been used to build the test structure used in the second phase. Fig. 7(b) represents in green the initial guess for the boron profile in the central region, while in red the extracted profile at the end of the procedure.

For comparison, Fig. 7(c) reports the result obtained by using a direct extraction from the C-V curve. In addition to the same limitations outlined for the 1D case, here it is visible a remarkable discrepancy between the reference and the extracted profiles. The reason can be ascribed to the edge effects, which play a significant role despite the size of the central area is not especially small (50-micron diameter). By contrast, from Fig. 7(b) it is evident how edge effects do not impact significantly on the quality of the profile extracted with the inverse method, as they are properly accounted for in the numerical model.

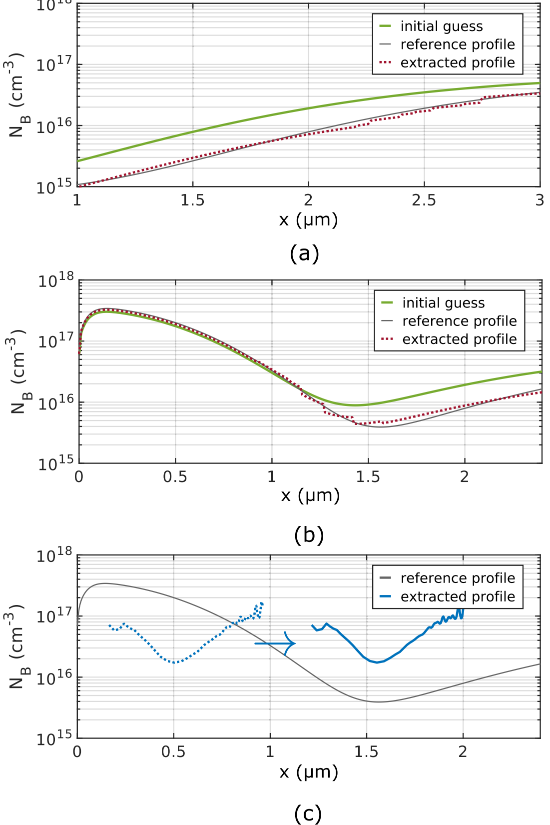

Fig. 7. Inverse doping profiling procedure applied to a 2D SPAD structure as in Fig. 4. In particular, (a) reports the lateral profile obtained during the first phase, in which the extraction procedure is applied to a device without the enrichment; (b) shows the central profile obtained at the end of the extraction procedure. For comparison, (c) reports the results of the direct extraction procedure before (dashed-blue) and after (solid blue) translation. The large error in the extracted profile is due manly to edge effects.

VI. Experimental Validation

A direct validation of the proposed method against experimental data is challenging because of the limited accuracy with which the doping profile can be measured in real devices. Actually, the limited accuracy in measuring certain doping profiles is exactly the reason that led us to develop this method. To bypass this problem, we used the extracted doping profile to calculate the breakdown voltage of the device under test and we compared it with the experimental value. Although this solution does not allow us to verify directly the accuracy of the extracted profile, nevertheless it represents a very significant test as the breakdown voltage is extremely sensitive to small variations in the doping profile, as shown for example in Section III-B.

To provide a convincing validation of the proposed method, we applied the procedure outlined above to a variety of devices characterized by different breakdown voltages and different electric field profiles, depending on the details of the fabrication process (e.g. implantation doses, thermal treatments, etc.). These devices belong to the two categories introduced in Section II, i.e. thin and red-enhanced SPADs, and have been fabricated by some of the authors at the Cornell NanoScale Science and Technology Facility (CNF), Cornell University, Ithaca (USA). The RE-SPADs have been extensively described in [53], while the structure and the performance of the thin SPADs are in line with those presented in [54].

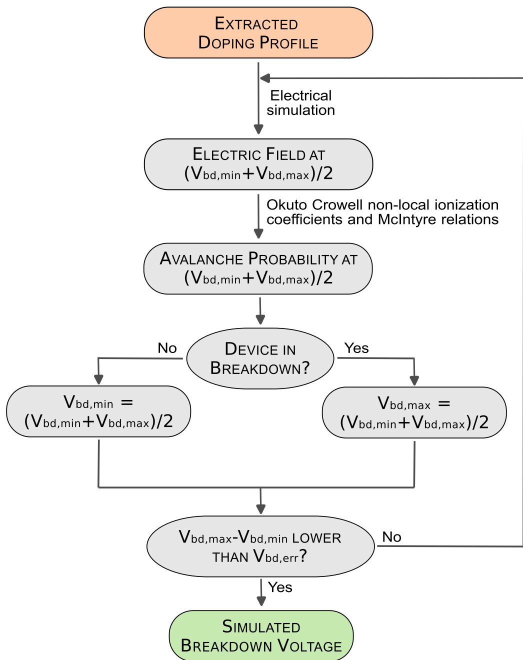

Fig. 8. Flowchart illustrating the calculation of the breakdown voltage V_{bd}: the interval $V_{bd,\min}$ - $V_{bd,\max}$ containing V_{bd} is progressively narrowed by using the bisection method until its amplitude becomes smaller than the preset error threshold $V_{bd,err}$.

Before discussing the methods applied to and the results obtained with RE- and thin SPADs, in the following sub-section we will briefly outline the procedure adopted for the calculation of the breakdown voltage from the extracted doping profiles.

A. Breakdown Voltage Calculation

Given the extracted doping profile, the breakdown voltage V_{bd} has been calculated by applying the bisection method on an interval, the upper and lower limits of which are respectively above and below the breakdown voltage. The procedure is illustrated in detail in Fig. 8. At each iteration, the electric field at the midpoint of the interval is calculated and used to evaluate if, at this voltage, the detector is in breakdown or not; the interval is then restricted accordingly. The procedure is iterated until the size of the interval allows to identify the breakdown voltage with an uncertainty lower than a preset threshold (typically 100 mV). To evaluate whether the detector is in breakdown or not, at each step of the iteration the avalanche probability is calculated. The device is considered in breakdown if, at the edge of the depleted region, this probability exceeds a preset threshold (typically 10^{-4}). However, the attained results are largely independent from the choice of the threshold value, given the steep increase of avalanche probability around the breakdown voltage. By contrast, the choice of the ionization coefficients is crucial for attaining accurate results. Indeed, in most silicon SPADs the multiplication field has a peaked shape with significant variations over a distance comparable with the dead space, i.e. the distance a carrier must travel to acquire an energy high enough to impact ionize. In these circumstances, the effect of the dead space must be considered explicitly by resorting to non-local ionization coefficients [55]. In particular, we adopted the model introduced by Okuto and Crowell in [56]. In this case the avalanche probability cannot be calculated with the relations introduced by Oldham et al. in [57], therefore we used the corresponding equations by McIntyre [58].

B. Thin SPADs

Thin-SPAD wafers used in this work contain test structures specifically designed for performing C-V measurements. They have the same doping profile as in regular SPADs, but with a square geometry having a side length of about 500 μm and rounded corners to avoid edge breakdown. Given the large dimension, the transition regions in the space charge at the edge of the enrichment and of the cathode give a negligible contribution to the overall capacitance. Thereby, the total capacitance C_{tot} has been modeled simply as the sum of two contributions, C_{enrich} and $C_{no-enrich}$, proportional respectively to the central area, where the enrichment is present, and to the lateral area, where the enrichment is absent. The specific contribution (i.e. per unit area) of $C_{no-enrich}$ has been assessed by performing C-V measurements on test structures with no enrichment, and has been subtracted from the measured C_{tot} in order to obtain C_{enrich}. As C_{enrich} corresponds to a uniform region, the doping profile has been extracted by using the 1D version of the algorithm described in Section IV-A. The breakdown voltages calculated from the extracted profiles are reported in Fig. 9 (blue box) and compared with experimental results. The breakdown error is smaller than 1 V for most of the SPADs and reaches a maximum of 1.59 V only for a detector in which the initial guess is especially far from the actual profile.

C. RE-SPADs

Differently from thin SPADs, the red-enhanced wafers used in this work did not contain test structures specific for C-V measurements. Therefore, the C-V measurements have been performed on regular SPADs and the doping profile has been extracted by using the 2D version of the algorithm described in Section IV-B. In particular, for the extraction of the lateral boron profile $N_{B,lateral}$, a 50 μm diameter SPAD has been used, in a modified version with no enrichment implantation. By contrast, during the second phase that leads to the extraction of the central boron profile, C-V measurements have been performed on SPADs with active diameters of 50, 100, 200, and 500 μm. The use of multiple diameters has allowed us to verify the robustness of the proposed method against different capacitance values and different contribution of the edge effects. To this regard, for the SPADs with the smaller diameters (i.e. 50 and 100 μm) a stray capacitance C_{stray} of some tens of femtofarads has a non-negligible effect on the extracted doping profile. This capacitance, due for example to the residual effects of package pins and connections to the LCR meter, can be assessed and subtracted from the C-V measurements before applying the extraction algorithm. A convenient option for the assessment is to notice that the SPAD capacitance reaches an almost constant value, once that the intrinsic layer has been fully depleted and the expansion of the space charge region is limited by the buried layer. As the position of the buried layer is typically known with good accuracy (thanks for example to SIMS measurements),

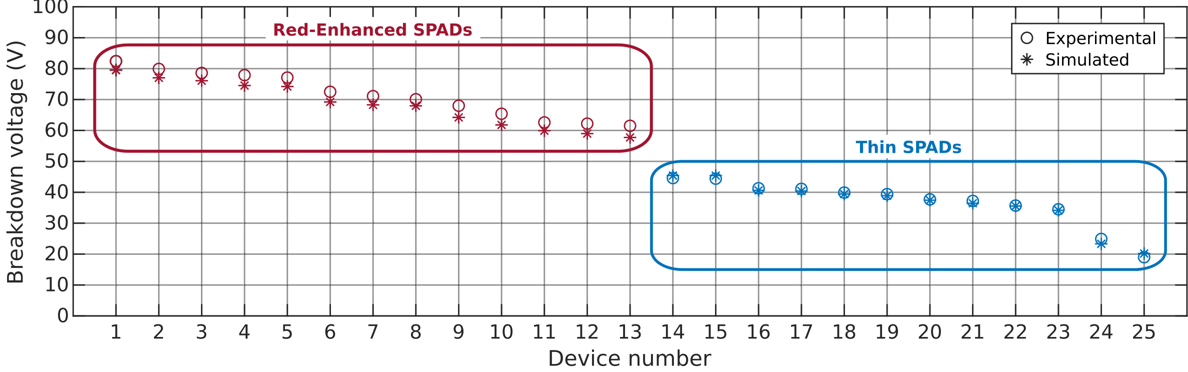

Fig. 9. Comparison between experimental and simulated breakdown voltages obtained from multiple thin and RE SPADs with different doping profiles.

and small changes do not impact significantly the results, this depletion capacitance can be calculated from device simulation. C_{stray} can be attained as the difference between the measured and the expected values of the capacitance at the higher voltages (i.e. when the intrinsic layer is fully depleted). By applying this procedure, we attained extracted profiles which are independent from the SPAD diameter in the range 50 – 500 μm.

From Fig. 9 it is possible to notice that a good matching between calculated and experimental breakdown voltages has been obtained also for RE-SPADs. Compared to thin SPADs, the error is larger, spanning from 2.13 and 3.78 V. This is a consequence of the thicker p- layer, which produces a larger deviation in the breakdown voltage given a certain error in the multiplication field [8]. However, for essentially the same reason, RE-SPADs are operated at higher overvoltages compared to thin SPADs, with typical values of 20 vs 5 V. Consequently, the larger error in the calculated breakdown voltage is of no concern from a practical point of view.

Finally, it's worth noting that the procedure for assessing C_{stray} described in this section cannot be easily applied to thin SPADs. In fact, in most thin SPADs the tails of the enrichment and buried layer profiles are partially overlapped, and there is not a clear region in which the capacitance does not change with the applied voltage. Therefore, the extraction procedure can be applied on small structures only with a setup in which the stray capacitance is well controllable and measurable.

VII. Discussion and Conclusion

The method presented in this article allows to extract an accurate profile of the doping concentration along a SPAD's depleted region. It starts from approximated data obtained from process simulations and SIMS measurements and refine it iteratively until the simulated C-V curve matches the one acquired experimentally. Such an inverse approach allows to overcome the limitations of the direct doping extraction from C-V data, and to fully benefit of the excellent sensitivity of this technique. Owning to the inherent nature of C-V measurements, the accuracy improvement in the doping profile is limited to the detector depleted region. This is actually the region where high accuracy is especially needed, because most SPADs metrics show a strong dependence on the electric field in the multiplication region. On the contrary, the accuracy provided by SIMS and process simulation is typically sufficient to characterize the doping profile in the quasi-neutral regions for the sake of SPAD modeling.

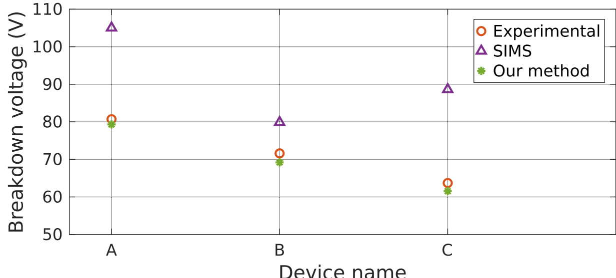

Fig. 10. Breakdown voltage of the three RE-SPADs indicated as A, B, and C. For each of them the breakdown voltage has been calculated using the procedure described in Section VI-A applied either to raw SIMS data (SIMS) or to the doping profile extracted by using the proposed method (Our method). The comparison with the experimental data (Experimental) shows that the proposed method provides a significant improvement compared to SIMS.

To verify the accuracy improvement provided by the proposed method compared to SIMS, we resorted again to the three RE-SPADs (namely A, B, and C) described in Section III-B. For each of them the breakdown voltage has been calculated starting from the raw SIMS data and from the profile extracted using the proposed method. Obtained results are reported in Fig. 10, along with experimental breakdown values. The benefit of refining SIMS data with the proposed inverse modeling scheme is clear.

As an application example, the method has been used to calculate the breakdown voltage of various SPADs characterized by different structures and doping profiles. As seen in Section VI, simulations results are in good agreements with experimental data. Two aspects makes these results especially interesting. On the one hand, the good matching has been obtained on a wide range of SPADs that includes different detector structures (thin and red-enhanced), breakdown voltages ranging from 18 to 84 V, and peak electric field from about 400 to 540 kV cm^{-1}. On the other hand, the good agreement between simulated and experimental breakdown-voltages has been obtained straight from the extracted profiles with no need of additional fitting procedures. In particular, the values of the ionization coefficients used for the calculation of the breakdown voltage are those originally proposed by Okuto and Crowell in [56]. This represents

an improvement compared to what has been previously reported for example in [59], where the carriers' mean free path has been modified to match the experimental breakdown voltage. Notably, in [59] the doping profile was obtained from SIMS measurements, and modified ionization coefficients provided good results only for thin SPADs. Taking all this into account, we believe that the proposed method may enable a truly predictive modeling of SPAD performance, which must not rely on case-by-case calibrations that are valid only on a limited range of detector designs.

Another interesting aspect is the fact that all the results reported in Fig. 9 have been obtained starting from the same two initial guesses, one for RE structures and the other one for thin devices. On the one hand, this shows that the method converges to the correct doping profile even starting from initial guesses that are relatively far from the actual profile; on the other hand, it means that only a few SIMS measurements may be sufficient to study a whole family of detectors, even characterized by considerably different peak electric fields and breakdown voltages.

Finally, the possibility of applying the proposed method not only to purposely developed test-structures, but also to real SPADs opens up some interesting opportunities. For example, the doping concentration across a wafer can be mapped more extensively, the measurements not being limited to the few regions where a suitable test-structure is available. Also, the possibility of measuring the doping profile in a specific detector allows to investigate possible second-order effects like the dependence of SPAD properties on the detector diameter or layout.

Although the implementation of the technique presented in this paper is specific for the two investigated SPAD structures, (RE and thin), the methodology is quite general, and we believe it can be adapted to other SPAD structures. However, some details of the algorithm (e.g. the extraction of the doping profile in the lateral regions) must be treated with a case-by-case approach to account for the presence of specific regions (e.g. doping wells, guard rings, etc.). The effectiveness of the method on a specific structure can be verified with a numerical validation, like the one presented in Section V.

In summary, we believe that the proposed method may represent a valuable tool in two distinct fields: on the one hand, it can support the development and validation of new and more accurate SPAD models; on the other hand, it can help troubleshooting possible issues like process non-uniformities.

References

[1] S. Cova, M. Ghioni, A. Lacaita, C. Samori, and F. Zappa, "Avalanche photodiodes and quenching circuits for single-photon detection," *Appl. Opt.*, vol. 35, no. 12, pp. 1956–1976, 1996.

[2] A. Pifferi et al., "New frontiers in time-domain diffuse optics, a review," *Proc. SPIE*, vol. 21, 2016, Art. no. 091310.

[3] D. Bronzi et al., "Automotive three-dimensional vision through a single-photon counting SPAD camera," *IEEE Trans. Intell. Transp. Syst.*, vol. 17, no. 3, pp. 782–795, Mar. 2016.

[4] H.-K. Lo, M. Curty, and K. Tamaki, "Secure quantum key distribution," *Nature Photon.*, vol. 8, no. 8, pp. 595–604, 2014.

[5] X. Michalet et al., "Silicon photon-counting avalanche diodes for single-molecule fluorescence spectroscopy," *IEEE J. Sel. Topics Quantum Electron.*, vol. 20, no. 6, pp. 248–267, Nov./Dec. 2014.

[6] K. Morimoto et al., "3.2 megapixel 3D-stacked charge focusing SPAD for low-light imaging and depth sensing," in *Proc. IEEE Int. Electron Devices Meeting*, 2021, pp. 20.2.1–20.2.4.

[7] E. V. Sieleghem et al., "A near-infrared enhanced silicon single-photon avalanche diode with a spherically uniform electric field peak," *IEEE Electron Device Lett.*, vol. 42, no. 6, pp. 879–882, Jun. 2021.

[8] A. Gulinatti et al., "New silicon SPAD technology for enhanced red-sensitivity, high-resolution timing and system integration," *J. Modern Opt.*, vol. 59, no. 17, pp. 1489–1499, 2012.

[9] M. Sanzaro et al., "Single-photon avalanche diodes in a 0.16 μm BCD technology with sharp timing response and red-enhanced sensitivity," *IEEE J. Sel. Topics Quantum Electron.*, vol. 24, no. 2, Mar./Apr. 2018, Art. no. 3801209.

[10] F. Nolet et al., "Quenching circuit and SPAD integrated in CMOS 65 nm with 7.8 ps FWHM single photon timing resolution," *Instruments*, vol. 2, no. 4, 2018, Art. no. 19.

[11] F. Gramuglia, M.-L. Wu, C. Bruschini, M.-J. Lee, and E. Charbon, "A low-noise CMOS SPAD pixel with 12.1 ps SPTR and 3 ns dead time," *IEEE J. Sel. Topics Quantum Electron.*, vol. 28, no. 2, Mar./Apr. 2022, Art. no. 3800809.

[12] F. Ceccarelli, A. Gulinatti, I. Labanca, M. Ghioni, and I. Rech, "Red-enhanced photon detection module featuring a 32×1 single-photon avalanche diode array," *IEEE Photon. Technol. Lett.*, vol. 30, no. 6, pp. 557–560, Mar. 2018.

[13] A. Ingargiola et al., "Multispot single-molecule FRET: High-throughput analysis of freely diffusing molecules," *PLoS One*, vol. 12, no. 4, 2017, Art. no. e0175766.

[14] B. Wunderlich et al., "Microfluidic mixer designed for performing single-molecule kinetics with confocal detection on timescales from milliseconds to minutes," *Nature Protoc.*, vol. 8, no. 8, pp. 1459–1474, 2013.

[15] R. Bedington, J. M. Arrazola, and A. Ling, "Progress in satellite quantum key distribution," *npj Quantum Inf.*, vol. 3, no. 1, 2017, Art. no. 30.

[16] J. Yin et al., "Satellite-based entanglement distribution over 1200 kilometers," *Science*, vol. 356, no. 6343, pp. 1140–1144, 2017.

[17] P. J. Clarke et al., "Analysis of detector performance in a gigahertz clock rate quantum key distribution system," *New J. Phys.*, vol. 13, no. 7, 2011, Art. no. 075008.

[18] J. L. O'brien, "Optical quantum computing," *Science*, vol. 318, no. 5856, pp. 1567–1570, 2007.

[19] E. A. Webster, J. A. Richardson, L. A. Grant, D. Renshaw, and R. K. Henderson, "A single-photon avalanche diode in 90-nm CMOS imaging technology with 44% photon detection efficiency at 690 nm," *IEEE Electron Device Lett.*, vol. 33, no. 5, pp. 694–696, May 2012.

[20] E. A. Webster, L. A. Grant, and R. K. Henderson, "A high-performance single-photon avalanche diode in 130-nm CMOS imaging technology," *IEEE Electron Device Lett.*, vol. 33, no. 11, pp. 1589–1591, Nov. 2012.

[21] F. Ceccarelli, A. Gulinatti, I. Labanca, I. Rech, and M. Ghioni, "Gigacount/second photon detection module based on an 8×8 single-photon avalanche diode array," *IEEE Photon. Technol. Lett.*, vol. 28, no. 9, pp. 1002–1005, May 2016.

[22] T. A. Abbas et al., "Backside illuminated SPAD image sensor with 7.83 μm pitch in 3D-stacked CMOS technology," in *Proc. IEEE Int. Electron Devices Meeting*, 2016, pp. 8.1.1–8.1.4.

[23] K. Ito et al., "A back illuminated 10 μm SPAD pixel array comprising full trench isolation and Cu-Cu bonding with over 14% PDE at 940 nm," in *Proc. IEEE Int. Electron Devices Meeting*, 2020, Art. no. 16.

[24] S. Shimada et al., "A back illuminated 6 μm SPAD pixel array with high PDE and timing jitter performance," in *Proc. IEEE Int. Electron Devices Meeting*, 2021, Art. no. 20.

[25] S. Shimada et al., "A SPAD depth sensor robust against ambient light: The importance of pixel scaling and demonstration of a 2.5 μm pixel with 21.8% PDE at 940 nm," in *Proc. Int. Electron Devices Meeting*, 2022, Art. no. 37.

[26] M.-J. Lee et al., "High-performance back-illuminated three-dimensional stacked single-photon avalanche diode implemented in 45-nm CMOS technology," *IEEE J. Sel. Topics Quantum Electron.*, vol. 24, no. 6, Nov./Dec. 2018, Art. no. 3801809.

[27] R. K. Henderson et al., "5.7 A 256×256 40 nm/90 nm CMOS 3D-stacked 120 dB dynamic-range reconfigurable time-resolved SPAD imager," in *Proc. IEEE Int. Solid-State Circuits Conf.*, 2019, pp. 106–108.

[28] X. Qian, W. Jiang, A. Elsharabasy, and M. J. Deen, "Modeling for single-photon avalanche diodes: State-of-the-art and research challenges," *Sensors*, vol. 23, no. 7, 2023, Art. no. 3412.

[29] M. A. Karami, M. Gersbach, H.-J. Yoon, and E. Charbon, "A new single-photon avalanche diode in 90 nm standard CMOS technology," *Opt. Exp.*, vol. 18, no. 21, pp. 22158–22166, 2010.
[30] W. Maes, K. D. Meyer, and R. V. Overstraeten, "Impact ionization in silicon: A review and update," *Solid-State Electron.*, vol. 33, no. 6, pp. 705–718, 1990.
[31] A. Schenk, "Rigorous theory and simplified model of the band-to-band tunneling in silicon," *Solid-State Electron.*, vol. 36, no. 1, pp. 19–34, 1993.
[32] G. Vincent, A. Chantre, and D. Bois, "Electric field effect on the thermal emission of traps in semiconductor junctions," *J. Appl. Phys.*, vol. 50, no. 8, pp. 5484–5487, 1979.
[33] M. Ghioni, A. Gulinatti, I. Rech, P. Maccagnani, and S. Cova, "Large-area low-jitter silicon single photon avalanche diodes," in *Proc. SPIE Quantum Sens. Nanophotonic Devices*, 2008, pp. 267–279.
[34] A. Gulinatti, P. Maccagnani, I. Rech, M. Ghioni, and S. Cova, "35 ps time resolution at room temperature with large area single photon avalanche diodes," *Electron. Lett.*, vol. 41, no. 5, 2005, pp. 272–274.
[35] M. Ghioni, A. Gulinatti, P. Maccagnani, I. Rech, and S. Cova, "Planar silicon SPADs with 200-μm diameter and 35-ps photon timing resolution," in *Proc. SPIE Adv. Photon Counting Techn.*, 2006, pp. 203–211.
[36] F. Ceccarelli et al., "Recent advances and future perspectives of single-photon avalanche diodes for quantum photonics applications," *Adv. Quantum Technol.*, vol. 4, no. 2, 2021, Art. no. 2000102.
[37] F. Ceccarelli, G. Acconcia, A. Gulinatti, M. Ghioni, and I. Rech, "83-ps timing jitter with a red-enhanced SPAD and a fully integrated front end circuit," *IEEE Photon. Technol. Lett.*, vol. 30, no. 19, pp. 1727–1730, Oct. 2018.
[38] D. K. Schroder, *Semiconductor Material and Device Characterization*. Hoboken, NJ, USA: Wiley, 2015.
[39] H. De Man, "On the calculation of doping profiles from C(V) measurements on two-sided junctions," *IEEE Trans. Electron Devices*, vol. 17, no. 12, pp. 1087–1088, Dec. 1970.
[40] D. Kennedy, P. Murley, and W. Kleinfelder, "On the measurement of impurity atom distributions in silicon by the differential capacitance technique," *IBM J. Res. Dev.*, vol. 12, no. 5, pp. 399–409, 1968.
[41] D. Kennedy and R. O'brien, "On the measurement of impurity atom distributions by the differential capacitance technique," *IBM J. Res. Dev.*, vol. 13, no. 2, pp. 212–214, 1969.
[42] W. Carter, H. Gummel, and B. Chawla, "Interpretation of capacitance vs. voltage measurements of pn junctions," *Solid-State Electron.*, vol. 15, no. 2, pp. 195–201, 1972.
[43] C. P. Wu, E. Douglas, and C. W. Mueller, "Limitations of the CV technique for ion-implanted profiles," *IEEE Trans. Electron Devices*, vol. 22, no. 6, pp. 319–329, Jun. 1975.
[44] M. Nishida, "Depletion approximation analysis of the differential capacitance—Voltage characteristics of an MOS structure with nonuniformly doped semiconductors," *IEEE Trans. Electron Devices*, vol. 26, no. 7, pp. 1081–1085, Jul. 1979.
[45] D. Bartelink, "Limits of applicability of the depletion approximation and its recent augmentation," *Appl. Phys. Lett.*, vol. 38, no. 6, pp. 461–463, 1981.
[46] W. C. Johnson and P. T. Panousis, "The influence of Debye length on the C-V measurement of doping profiles," *IEEE Trans. Electron Devices*, vol. 18, no. 10, pp. 965–973, Oct. 1971.
[47] G. Ouwerling, "Physical parameter extraction by inverse device modelling: Application to one-and two-dimensional doping profiling," *Solid-State Electron.*, vol. 33, no. 6, pp. 757–771, 1990.
[48] N. Khalil, J. Faricelli, D. Bell, and S. Selberherr, "The extraction of two-dimensional MOS transistor doping via inverse modeling," *IEEE Electron Device Lett.*, vol. 16, no. 1, pp. 17–19, Jan. 1995.
[49] N. Khalil, J. Faricelli, D. Bell, and S. Selberherr, "A novel method for extracting the two-dimensional doping profile of a sub-half micron MOSFET," in *Proc. VLSI Technol. Symp.*, 1994, pp. 131–132.
[50] G. Ouwerling, J. Staalenburg, and M. Kleefstra, "Electrical characterization of 2-D doping profiles," in *Proc. Int. Conf. Microelectron. Test Structures*, 1990, pp. 3–8.
[51] C. Chiang and Y. Yeow, "Inverse modeling of two-dimensional MOSFET dopant profile via capacitance of the source/drain gated diode," *IEEE Trans. Electron Devices*, vol. 47, no. 7, pp. 1385–1392, Jul. 2000.
[52] N. Khalil, J. Faricelli, C.-L. Huang, and S. Selberherr, "Two-dimensional dopant profiling of submicron metal–oxide–semiconductor field-effect transistor using nonlinear least squares inverse modeling," *J. Vac. Sci. Technol. B: Microelectronics Nanometer Structures Process. Meas. Phenomena*, vol. 14, no. 1, pp. 224–230, 1996.
[53] A. Gulinatti, F. Ceccarelli, M. Ghioni, and I. Rech, "Custom silicon technology for SPAD-arrays with red-enhanced sensitivity and low timing jitter," *Opt. Exp.*, vol. 29, no. 3, pp. 4559–4581, 2021.
[54] M. Ghioni, A. Gulinatti, I. Rech, F. Zappa, and S. Cova, "Progress in silicon single-photon avalanche diodes," *IEEE J. Sel. Topics Quantum Electron.*, vol. 13, no. 4, pp. 852–862, Jul./Aug. 2007.
[55] Y. Okuto and C. Crowell, "Ionization coefficients in semiconductors: A nonlocalized property," *Phys. Rev. B*, vol. 10, no. 10, 1974, Art. no. 4284.
[56] Y. Okuto and C. Crowell, "Energy-conservation considerations in the characterization of impact ionization in semiconductors," *Phys. Rev. B*, vol. 6, no. 8, 1972, Art. no. 3076.
[57] W. G. Oldham, R. R. Samuelson, and P. Antognetti, "Triggering phenomena in avalanche diodes," *IEEE Trans. Electron Devices*, vol. 19, no. 9, pp. 1056–1060, Sep. 1972.
[58] R. McIntyre, "A new look at impact ionization-Part I: A theory of gain, noise, breakdown probability, and frequency response," *IEEE Trans. Electron Devices*, vol. 46, no. 8, pp. 1623–1631, Aug. 1999.
[59] A. Gulinatti et al., "Modeling photon detection efficiency and temporal response of single photon avalanche diodes," in *Proc. SPIE Photon Counting Appl. Quantum Opt. Quantum Inf. Transfer Process.*, 2009, pp. 161–177.

Andrea Bonzi received the B.Sc. and M.Sc. degrees (with a mark of 110/110 and 110/110 *cum laude*)in electronics engineering from the Politecnico di Milano, Milan, Italy, in 2017 and 2020, respectively. Since 2020, he has been working toward the Ph.D. degree in information technology with the Dipartimento di Elettronica, Informazione e Biongegneria, Politecnico di Milano. His main research interests related to single-photon detectors and their applications.

Gabriele Laita received the B.Sc. degree (*cum laude*) and the M.Sc. degree (*cum laude*) in electronics engineering, from the Politecnico di Milano, Milano, Italy, in 2019 and 2022, respectively. Since 2022, he has been working toward the Ph.D. degree in information technology with the Dipartimento di Elettronica, Informazione e Bioingegneria, Politecnico di Milano. His research focuses on directed toward high detection efficiency SPADs.

Ivan Rech (Senior Member, IEEE) received the M.S. degree in electronic engineering and the Ph.D. (with Hons.) degree in information technology from the Politecnico di Milano, Milan, Italy, in 2000 and 2004, respectively. He is currently an Associate Professor with the Politecnico di Milano. He was involved in several interdisciplinary research projects on molecular biology, quantum cryptography, adaptive optics in astronomy, and developing dedicated instrumentation. His research interests include the development of single photon detectors and associated electronics for biomedical, genetic, and diagnostic applications.

Angelo Gulinatti (Member, IEEE) received the M.Sc. degree (*cum laude*) in electronics engineering and the Ph.D. degree (*cum laude*) in information technology from the Politecnico di Milano, Milan, Italy, in 2003 and 2007, respectively. Since 2008, he has been with Dipartimento di Elettronica, Informazione e Bioingegneria of Politecnico di Milano, firstly as Assistant Professor and currently as an Associate Professor. From 2013 to 2017, he was a Visiting Scientist with the Cornell NanoScale Science and Technology Facility, Cornell University, Ithaca, NY, USA. He has coauthored more 100 papers published in peer-reviewed journals and in conference proceedings. His research interests include the development of custom technology SPADs and related electronics for applications ranging from biochemistry to quantum information processing.